



Simulation-Based Fracture Assessment of Seismic Moment Frame Connections with Box Columns

Hiroshi Yasumoto, S.M.ASCE¹; Amit Kanvinde, M.ASCE²; Chia-Ming Uang, M.ASCE³; and Rupa Garai, M.ASCE⁴

Abstract: Welded connections between beams and built-up box columns in steel moment frames require the attachment of continuity plates to the inside of the column using complete-joint-penetration (CJP) groove welds. Electroslag welding (ESW) is often used to weld at least one of the four sides of each continuity plate to the inside of the box column. These welds are susceptible to fracture due to decreased material toughness and installation of containment plates that create a notch condition. Finite-element simulations are presented to examine the effect of design and detailing parameters on the fracture of these connections, as assessed through conventional fracture mechanics as well as continuum damage mechanics. The results indicate that improved bevel details in the containment plate and reduced beam section (RBS) connections strongly mitigate fracture demands, whereas both eccentricity in the weld with respect to the continuity plate and unequal beam and column flange widths exacerbate demands. The beam and column size, as well as beam web weld access hole details, have only a modest effect on the demands. Simulations are also conducted to examine column-wall thickness limits beyond which continuity plates may not be required. These suggest that limits similar to those specified for wide-flanged columns may not provide adequate performance. Limitations of the study are presented, along with directions for future work. DOI: 10.1061/JSENDH.STENG-13042. © 2024 American Society of Civil Engineers.

Author keywords: Box columns; Fracture; Welded connections.

Introduction

Built-up box columns are used in seismically designed steel moment frames (SMFs) to resist biaxial bending and to provide economy in meeting seismic strength and drift requirements in an economical manner, in comparison with rolled wide-flanged (i.e., W-) sections. Although they are increasingly popular, especially for high-rise steel buildings in seismic regions, some factors limit their widespread use in the US. These columns are usually constructed from plate steel with longitudinal complete-joint-penetration (CJP) welds (which are required in the region near the connection) to form the box. A key issue, which is the focus of this paper, pertains to the beam-to-column connections in these columns. Fig. 1(a) shows a typical beam-to-column connection used in such columns.

Referring to Fig. 1(a), a continuity or diaphragm plate (similar to that provided in conventional beam-to-W-section column connections) is usually provided to effectively transfer the forces introduced by the beam flange into the column face plate. The continuity plate presents a fabrication challenge because it must be attached to all four sides of the box from the inside using CJP

Note. This manuscript was submitted on July 27, 2023; approved on November 28, 2023; published online on February 21, 2024. Discussion period open until July 21, 2024; separate discussions must be submitted for individual papers. This paper is part of the *Journal of Structural Engineering*, © ASCE, ISSN 0733-9445.

welds. Conventional welding techniques cannot be used on all four sides of the continuity plate because access to the inside of the box column is not available once the box is closed. Electroslag welding (ESW) has been proposed as a solution to this problem. Figs. 1(b and c) schematically illustrate the process for installation of the continuity plate within the box column using the ESW technique.

As shown in Fig. 1, three sides of the box are first welded together; this is accomplished by introducing longitudinal welds along the length of these plates. These longitudinal welds are required to be CJP in the vicinity of the beam-column connection but permitted to be partial-joint-penetration (PJP) welds elsewhere along the length. Then, the continuity plate is CJP-welded to three sides of the box using flux-cored arc welding (FCAW) before the fourth plate is welded to close the box. This leaves the fourth side of the continuity plate unattached to the box plate. To attach this plate to the box wall, the ESW technique is employed, as shown in Fig. 1(c). This involves inserting an electrode through a hole in an adjacent column face plate, and then depositing weld filler material between the continuity plate and the box plate. The electrode is gradually raised as the filler material is deposited in a single weld pass, until the entire length of the continuity plate is CJP-welded to the box plate. The electrode is continuously fed into the rising weld pool in the joint.

Padilla-Llano and Ocel (2021) and Gilmer (2005) have given a historical overview of the development and use of the ESW process. Although the ESW process overcomes the fabrication challenges outlined in the preceding paragraphs, it raises other issues from the standpoint of structural performance of the beam-column connections. These issues are related to two factors:

 The extremely high weld deposition rates (on the order of ~20 kg/h, relative to 1–4 kg/h commonly seen in conventional FCAW welds) result in heat input on the order of 10 times that of FCAW welds, along with low cooling rates that result in wide heat-affected zones (HAZs) with coarse-grained microstructures.

¹Engineer, Kobori Research Complex, Kajima Corporation, 6-5-30, Akasaka, Minato-ku, Tokyo 107-8502, Japan.

²Professor, Dept. of Civil and Environmental Engineering, Univ. of California, Davis, CA 95616 (corresponding author). Email: kanvinde@ucdavis.edu

³Professor, Dept. of Structural Engineering, Univ. of California, San Diego, La Jolla, CA 92093.

⁴Senior Associate Principal, Skidmore Owings and Merrill, 1 Maritime Plz, San Francisco, CA 94111.

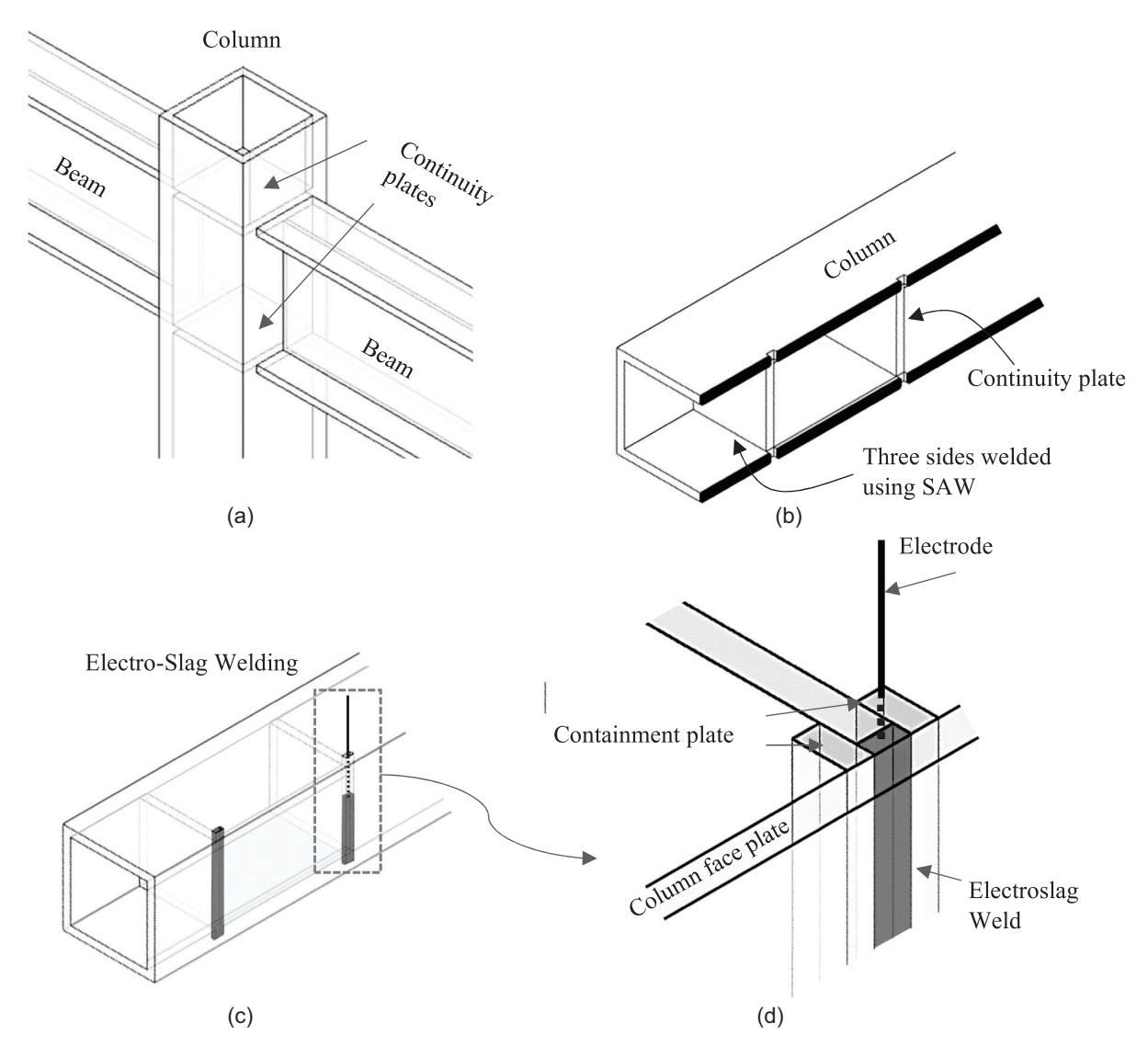


Fig. 1. Fabrication of beam-box-column connection: (a) overview; (b) welding on three sides of continuity plate; (c) ESW welding on fourth side after closing box; and (d) detail of ESW weld process.

This ultimately leads to decreased material toughness in these welds.

 The ESW joints entail attachment of containment plates on the inside of the box [Fig. 1(d)] to contain the weld pool as the filler metal is deposited. These typically lead to stress concentrations or notch conditions due to lack-of-fusion regions or re-entrant corners.

The combination of the decreased material toughness and the discontinuities in weld regions raises concerns regarding the seismic performance of these connections, such that there are significant restrictions in design standards regarding their use. Specifically, AISC 358-22 (AISC 2022a) disallows the use of built-up box columns that have either a depth or width greater than 24 in. (588 mm), and reduced beam section (RBS) beams that are larger than W36 \times 300. Additionally, AISC 358-22 indicates (in its commentary) that "where moment frame beams do not connect to all four sides of the box column, it is recommended that the ESW side of the column be located where there is no moment frame."

Moreover, seismic design codes, including AISC 358 as well as the *Seismic Provisions*, i.e., AISC 341 (AISC 2022b) do not provide guidance regarding when the continuity plate need not be specified. This contrasts with beam-to-W-section column connections

for which clear guidance exists. Designers must either adapt such guidance to box columns or conservatively specify continuity plates, resulting in the aforementioned problems with the ESW joint. Collectively, these considerations constrain the effective use of box sections to economically design SMFs. As a result, development of technologies and details that mitigate these problems has been of interest to researchers and professional communities internationally (Lin et al. 2012; Tsai et al. 2020).

Nonetheless, the research in this area is somewhat limited, relative to other similar structural details. Specifically, in the US, only one test program (Ozkula et al. 2019) has been conducted, in which only one out of three experiments showed acceptable response, i.e., met prequalification standards (AISC 341-22). Previous testing in Taiwan (Lin and Jhuang 2010) included 22 experiments, of which 12 showed premature failure. These results, in part, have contributed to the current guidelines. Developing robust provisions to support the use of beam-to-box-column connections requires research and synthesis on the following fronts: (1) understanding fracture toughness demands or continuum damage mechanics based demands (generically termed fracture demands) in these connections, and the effect of various detailing and geometric parameters on these demands, (2) the development of welding

and fabrication technologies that provide adequate toughness to meet these demands, and (3) large-scale qualification testing to demonstrate connection performance.

This paper addresses the first of these through continuum finite element (CFE)-based fracture mechanics simulations to examine the effect of detailing considerations and parameters on internal stress distributions and fracture demands in beam-to-box-column connections. These include different types of containment plate configurations, beam and column dimensions (section sizes, wall thicknesses, weld access hole geometry, and the use of a reduced beam column, i.e., RBS details) as well as continuity plates sizes, with the objective to develop insights that may be used to support effective details for such connections. Additionally, the sensitivity of results to material fracture resistance is also assessed. The paper begins by providing background regarding relevant research in the area that has a direct bearing on the simulations conducted in this study. This is followed by a description of the CFE simulation methodology, including the fracture mechanics approaches used. The effect of each parameter is then examined in the context of prospective connection detailing strategies. The paper concludes by outlining limitations of the study and providing directions for future work.

Background and Previous Work

Research on ESW joints and their application to box-column continuity plate welds has been a focus of research internationally. In the US, qualification testing on box-column connections has been conducted in support of a 24-story building in San Diego (Ozkula et al. 2019). This testing featured three RBS moment connections attached to 24 in. $(610 \text{ cm}) \times 36$ in. (914 mm) built-up steel box columns. Figs. 2(a and b) schematically illustrate the ESW details used in these connections to connect the continuity plate to the box column. It can be seen that two types of containment plate details were used: (1) a conventional detail [Fig. 2(a)], and (2) an improved detail, mitigating the notch condition of the conventional detail [Fig. 2(b)]. The detail shown in Fig. 2(b) also includes shim plates between the containment plate and the continuity plate, intended to cool the weld more effectively.

Two of these specimens [termed Specimens 1 and 2 by Ozkula et al. (2019)] with the conventional bevel detail [such as shown in Fig. 2(a)] suffered brittle fracture at story drift ratios below 4.0%

(which is usually required for connection prequalification) under an applied cyclic loading protocol (AISC 341-22), whereas Specimen 3 with the improved bevel detail [similar to Fig. 2(b)] survived the applied protocol through cycles corresponding to 4% drift without significant strength deterioration, meeting the standard for prequalification.

Fig. 2(c) shows another type of beveled detail developed by Lin et al. (2012) in Taiwan, mitigating the notch condition of conventional detail. Such beveling moves the notch tip out of the path of direct stresses under the beam flange, reducing fracture demands. Figs. 3(a and b) show the posttest ESW joint region, indicating the weld and containment plate, as well as the cracking/fracture observed in Specimens 2 and 3 of the Ozkula et al. (2019) tests, hereafter referred to as the University of California, San Diego (UCSD), tests. Figs. 3(a and b) indicate the notch condition introduced by the containment plates, at which cracks initiated under the applied load, as well as some other features of interest. Referring to Fig. 3(a), the cracking that initiated at the notch resulted in this connection being completely severed. On the other hand, the specimen with the improved detail [Fig. 3(b)] showed the initiation of cracking at the notch but without brittle propagation.

Significant research on ESW connections has also been conducted in Japan and Taiwan. Lin and Jhuang (2010) reported a statistical evaluation of 22 box-column moment frame connections and determined that 12 of these specimens did not achieve the 4% story drift angle requirement for SMFs. Similar research conducted in Japan led to the publication of a guidebook (JSSC 2016). The guidebook outlines a simplified fracture mechanics—based method for the design of ESW box-column connections, accounting for the through-thickness stresses in the column face plate.

Work by Chen et al. (2009) and more recently Tsai et al. (2020) and Chen et al. (2020) used CFE simulations to assess the effects of parameters on local strain and fracture demands. Of these, Chen et al. (2009) determined through finite-element simulation that the welding defect at the containment plate significantly raised stresses and fracture toughness demands in the connection. Tsai et al. (2020) reported results of two subassembly tests, establishing cumulative plastic strain based damage mechanics as a useful tool for predicting fracture in ESW box-column connections. Additionally, they determined that the relative eccentricity (or misalignment) between the beam flange and the ESW joint results in very high fracture toughness demands, and that these demands may be

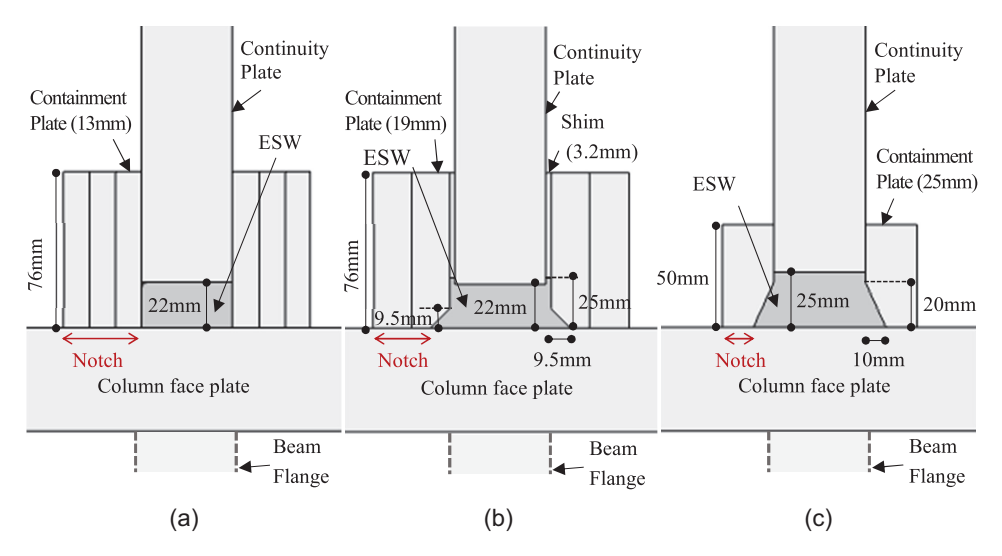


Fig. 2. Electroslag weld joint detail: (a) standard, S; (b) beveled detail, B1; and (c) beveled detail, B2.

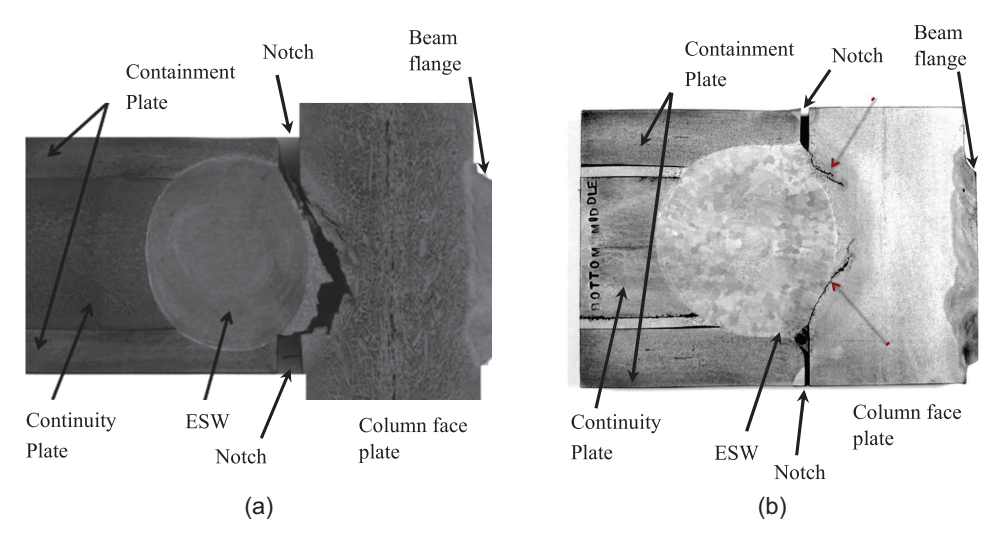


Fig. 3. Electroslag weld joint after testing: (a) Test 2; and (b) Test 3 from the UCSD test series.

mitigated by enlarging the radius of the ESW joint. Chen et al. (2020) expanded these findings through parametric finite-element analysis, noting that ESW weld bulb diameters have a stronger effect on fracture compared with eccentricities or thickness of the diaphragm plates. Cumulatively, this research indicates that boxcolumn moment connections with ESW diaphragm welds require serious innovation, research, and guideline development for more widespread use in construction, in the US as well as overseas.

Overall Methodology and Simulation Matrix

The primary objective of this study is to examine fracture demands in variations of box-column moment connections through CFE simulations. Consequently, the overall methodology includes three parts, illustrated in Fig. 4. The main research component comprises CFE simulations to relate externally applied loading to fracture demands at critical locations within the structural component. The CFE models use inputs that pertain to detail configuration and geometry as well as material properties, and rely on conventional

as well as damage mechanics—based fracture criteria for interpretation of the results. This section addresses the various input parameters and effects examined through the CFE simulations that are described in detail in the next section.

Tables 1 and 2 summarize the simulations conducted. Specifically, Table 1 presents the simulation matrix for the moment connections with the internal continuity plate and ESW joints, whereas Table 2 illustrates simulations designed to examine the necessity of the continuity plate itself, depending on the column-wall plate thickness and other factors. In these, no ESW joint is present, and the fracture critical location is on the outside of the column in the CJP groove weld between the beam bottom flange and the column. Because these simulations (and their purpose) are functionally different from the ESW simulations, a separate simulation matrix is formulated for them. Referring to the Table 1, a total of 14 simulations were conducted for the ESW joint, interrogating the following parameters:

Containment plate detail. Three details were considered; these
include a standard containment plate detail without any bevel as
shown in Fig. 2(a) (denoted S), and two beveled details (denoted

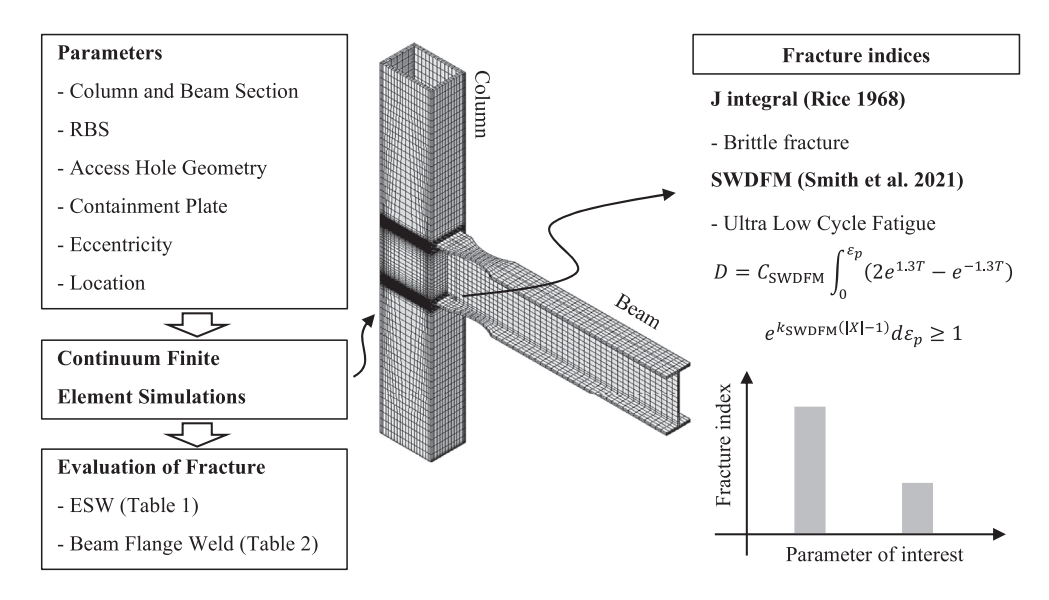


Fig. 4. Schematic illustration of methodology.

Table 1. Simulation matrix for ESW box-column moment connections with continuity plate

					Containment			Drift when $D = 1$ (%)			P_f at 4%
No.	Column	Beam section	Access hole	$Z_{\rm RBS}^{a}/Z_{X}^{b}$	plate	Eccentricity, e	b_{bf}^{c}/b_{cf}^{d}	Web	BE	CC	(%)
1	610×914	$W36 \times 302$	AWS D1.8	1.0 ^a	S	0	0.70	0.75	_	_	3.0
2	610×914	$W36 \times 302$	AWS D1.8	1.0^{a}	B1	0	0.70	3.00	1.00	_	0.0
3	610×914	$W36 \times 302$	AWS D1.8	1.0^{a}	S	10	0.70	0.50	_	_	84
4	610×914	$W36 \times 302$	AWS D1.8	1.0 ^a	B1	10	0.70	0.75	_	_	7.2
5	610×914	$W36 \times 302$	AWS D1.8	0.76	B1	0	0.70	4.00	_	_	0.0
6	610×914	$W36 \times 302$	AWS D1.8	0.62	B1	0	0.70	5.00	1.50	_	0.0
7	610×914	$W36 \times 302$	AISC360	1.0 ^a	B1	0	0.70	2.00	_	_	0.0
8	610×914	$W27 \times 368$	AWS D1.8	1.0^{a}	B1	0	0.74	2.00	1.00	—	0.1
9	610×914	$W27 \times 368$	AWS D1.8	1.0^{a}	S	0	0.74	0.75	_	_	6.0
10	610×914	$W27 \times 368$	AISC360	1.0^{a}	B1	0	0.74	2.00	_	—	0.1
11	610×914	$W36 \times 302$	AWS D1.8	1.0^{a}	B2	0	0.70	2.00	_	—	0.3
12	610×610	$W36 \times 302$	AWS D1.8	0.62	B1	0	0.70	6.00	2.00	_	0.0
13	432×914	$W36 \times 302$	AWS D1.8	0.62	B1	0	1.0	<i>D</i> < 1	<i>D</i> < 1	_	0.0
14	762×914	$W36 \times 302$	AWS D1.8	0.62	B1	0	0.56	4.00	2.00	5.00	0.0

Note: Unit = mm; and t_{cf} = column-flange thickness = 50.8.

Table 2. Simulation matrix to examine the necessity of continuity plate

No.	${t_{cf}}^{ m a}$	Beam section	${b_{bf}}^{ m b}$	$t_p^{\ c}/t_{bf}^{\ d}$	Containment plate	$rac{t_{cf}}{t_{cf-WF}^{ m AISC}}$ e	$D_{4\%}{}^{ m f}$
16	50.8	W36 × 302	427	1.0	B1	0.71	0.76
17	50.8	$W36 \times 302$	427	0.52	B1	0.71	1.92
18	50.8	$W36 \times 302$	427	_	Without	0.71	54
19	76.2	$W36 \times 302$	427	1.0	B1	1.06	0.68
20	76.2	$W36 \times 302$	427	0.52	B1	1.06	0.93
21	76.2	$W36 \times 302$	427	_	Without	1.06	2.25
22	127	$W36 \times 302$	427	1.0	B1	1.76	0.45
23	127	$W36 \times 302$	427	0.52	B1	1.76	0.49
24	127	$W36 \times 302$	427	_	Without	1.76	0.59
25	50.8	$W27 \times 368$	630	1.0	B1	0.62	0.67
26	50.8	$W27 \times 368$	630	0.50	B1	0.62	1.33
27	50.8	$W27 \times 368$	630	_	Without	0.62	5.8
28	76.2	$W27 \times 368$	630	1.0	B1	0.93	0.48
29	76.2	$W27 \times 368$	630	0.50	B1	0.93	0.64
30	76.2	$W27 \times 368$	630	_	Without	0.93	2.13
31	127	$W27 \times 368$	630	1.0	B1	1.55	0.37
32	127	$W27 \times 368$	630	0.50	B1	1.55	0.40
33	127	$W27 \times 368$	630	_	Without	1.55	0.54
34	102	$W36 \times 302$	427	1.0	B1	1.41	0.53
35	102	$W36 \times 302$	427	0.52	B1	1.41	0.60
36	102	$W36 \times 302$	427	_	Without	1.41	0.97
37	152	$W36 \times 302$	427	1.0	B1	2.12	0.39
38	152	$W36 \times 302$	427	0.52	B1	2.12	0.40
39	152	$W36 \times 302$	427	_	Without	2.12	0.43

 $_{cf}^{a}t_{cf}$ = column-flange thickness.

B1 and B2). Of these, B1 [Fig. 2(b)] refers to a detail used for Specimen 3 in the UCSD testing, which includes a bevel within the containment plate to minimize the notch effect, in addition to the introduction of a shim plate whose purpose is to cool the ESW efficiently. B2 was developed by Lin et al. (2012) in

Taiwan, which includes the bevel but not the shim plate. The thicknesses of the containment and shim plates are 18 mm (3/4 in.) and 3.2 mm (1/8 in.), respectively. The introduction of the shim plate affects the heat transfer during the welding process, ultimately altering the local material properties in a

 $^{^{}a}Z_{RBS}$ = plastic section modulus of RBS section.

 $^{{}^{\}rm b}Z_X$ = plastic section modulus of the unreduced beam.

 $^{{}^{}c}b_{bf}$ = beam-flange width.

 $^{{}^{\}rm d}b_{cf}$ = column-flange width.

 $^{{}^{\}rm b}b_{bf}^{\rm j}$ = beam-flange width.

 $^{{}^{}c}t_{p} = \text{continuity-plate thickness.}$

 $^{{}^{\}rm d}t_{bf}$ = beam-flange thickness.

 $^{{}^{\}rm e}t_{cf-WF}^{\rm AISC}$ = AISC limit on column-flange thickness beyond which continuity plates are needed.

 $^{^{}f}D_{4\%}$ = damage at 4% drift.

favorable way. Although the simulations in this study simulate the geometric effect of the shim plate and the containment plate, the effect on material properties was not simulated.

- Effect of beam and column sizes. Referring to Table 1, two beam sizes (W36 × 302 and W27 × 368), along with four column sizes were used.
- Effect of using a RBS in the beam. Two levels of beam-flange reduction were used in addition to an unreduced flange, i.e., a welded unreinforced flange- welded web (WUF-W) connection, following the geometric requirements of AISC 358-22's Section 5.8; these include flange reductions of 67 mm (2.625 in.) and 105 mm (4.125 in.) flange reductions [Fig. 5(a)]. These RBS configurations (denoted RBS1 and RBS2) represent a reduction in the effective plastic modulus to 76% and 62%, respectively, with respect to a WUF-W connection (i.e., unreduced flange). The RBS mitigates stress demands in the connection at the column face and at the ESW joint. This was one of the strategies pursued by Ozkula et al. (2019) to successfully achieve ductile performance (i.e., attainment of 0.04 radians drift without failure) in their experimental program.
- Weld access hole (WAH) geometry. Two geometries for the WAH were used; these include the geometric requirements of AISC 360's Fig. C-J1.2 (AISC 2022c) and a larger web access hole geometry, based on American Welding Society (AWS) D1.8 (AWS 2016). Fig. 5(b) shows the two weld access hole geometries; these are termed Standard and Improved, respectively.
- Eccentricity of ESW weld bulb. The electrode moves laterally within the containment plates as it is being retracted vertically during the welding process, sometimes resulting in an unintended eccentricity that exacerbates the notch effect. This was observed in one of the UCSD specimens (Specimen 2). Moreover, the eccentricity of the weld bulb was identified to be an important issue during previous CFE simulations by Chen et al. (2020) and Tsai et al. (2020). Fig. 5(c) illustrates the definition of the eccentricity parameter, denoted e. Two values of e, i.e., e = 0 and e = 10 mm, were examined in this study based on the measured eccentricity in UCSD Specimen 2. The eccentricity was assumed to be constant through the entire length of the ESW weld. In both cases, the continuity plate and the beam flange were perfectly aligned; the issue of misalignment between these is a distinct matter and has been examined previously by Chen et al. (2020).

Referring to Table 1, the simulation matrix is fractional-factorial. This means that although the effect of each aforementioned

parameter is examined, all possible cross-dependencies are not examined. However, subsets of the simulations may be used to isolate the effects of individual parameters. Referring to Table 2, additional simulations were conducted to examine the necessity of the continuity plate itself, considering that (1) provisions governing the use of such plates for box columns do not yet exist, and (2) removing the continuity plate will eliminate the entire problem associated with the ESW joint.

However, the absence of the continuity plate influences the fracture potential in the beam-flange CJP-groove weld on the outside of the column face plate. This is because the continuity plate constrains out-of-plane bending of the column face plate when loaded by the beam flange and mitigates stress concentrations in the beam-flange groove weld. Thus, these simulations examine a different issue compared with those in Table 1. The relevant parameters expected to influence the continuity plate are the beam-flange thickness and the column thickness, and the ratio between the width of the beam flange and the column flange, i.e., b_{fb}/b_{fc} . The AISC 360 specifications (AISC 2022a, b, c) indicate that continuity plates are required unless the column flange thickness is greater than the following:

$$t_{cf-WF}^{\text{AISC}} = \max\left(0.4\sqrt{1.8b_{bf}t_{bf}\frac{F_{yb}}{F_{yc}}}, \frac{b_{bf}}{6}\right)$$
 (1)

where b_{bf} and t_{bf} = beam-flange width and thickness; and F_{yb} and F_{yc} = expected yield strengths of the beam and column, respectively. Although Eq. (1) is not prescribed for box columns, the aforementioned implied thickness is used here as a reference value to interpret simulation results. Table 2 provides the ratio between the column flange thickness and the threshold thickness shown previously. The thickness of the continuity plate (normalized by the beam-flange thickness) is also given. For a single-sided connection (as analyzed in this study), the minimum required continuity plate thickness is $0.5t_{bf}$.

Continuum Finite-Element Models

Each of the parameter sets defined in Tables 1 and 2 was examined through CFE simulations to assess the fracture demands at critical locations in the connections. The simulations were conducted using the software ABAQUS version 2020 as nonlinear static analyses and share some features in terms of overall methodology, constitutive

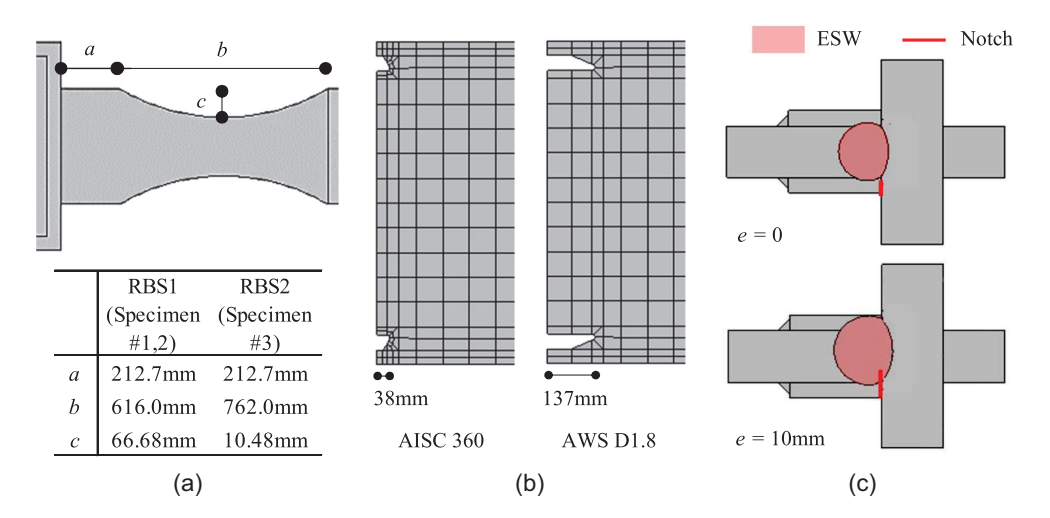


Fig. 5. Continuum finite element models: (a) RBS geometry; (b) WAH geometry; and (c) weld electrode eccentricity.

material models, and fracture indices used, but are different in other aspects, specifically those pertaining to their geometric construction and meshing. No convergence issues were observed in any of the simulations. The following subsections summarize each set of simulations before describing the features common to both. The calibration of material properties for each of these are discussed in a subsequent section. More details regarding the simulations, including additional results, have been given by Yasumoto (2023).

Simulations to Examine Fracture Demands at the ESW Joint

The parameter sets indicated in Table 1 may be arranged in a hierarchy wherein some share identical global characteristics (e.g., beam size and RBS ratio, column size, and continuity plate thickness) but differ at a local detailing level, i.e., containment plate configuration or ESW eccentricity. To simulate these various conditions with computational efficiency, a global model-submodel scheme was used, which is illustrated in Fig. 6. This scheme includes two steps:

- 1. Three-dimensional CFE models of the complete connection configuration including the beam, column, and continuity plate are constructed for each of the global parameter sets and subjected to loadings and boundary conditions to reflect component-level actions (e.g., story drifts). This is shown in Fig. 6 for one of the simulations, i.e., Simulation 6, which is complementary to Specimen 3 from the UCSD test program.
- 2. Submodels are then created to reflect the local detailing. The submodels [Fig. 6(b)] are driven by the displacements computed from the global models and feature fine meshes and notch or crack-tip geometries to compute stresses and strains at resolutions required to characterize fracture demands. This is a well-established procedure such that ABAQUS provides on-board capabilities for submodeling.

This approach results in significant computational efficiency because (1) it allows for fine meshing of critical regions of interest whereas the global model may be meshed coarsely without the associated problems of mesh transition, and (2) it allows for a limited number of global model runs, for which numerous submodel runs

may be conducted to interrogate local effects, e.g., by altering submodel details or by inserting the submodels at different locations within the overall component.

The global model was constructed to reflect all aspects of the overall geometry of the beam-column subassemblage, including 9.14 m of the beam and 4.88 m of the column, which is consistent with a typical story height and bay width. A single-sided connection was used in this study. Pinned boundary conditions (applied in the form of knife-edge displacements) were applied at the top and bottom of the column segment; these are indicated in Fig. 6. Two types of loading were applied to each model: (1) upward monotonic displacement at the beam-tip up to an equivalent drift of 6%; this produced tension in the lower flange, and (2) cyclic displacement history at the beam tip as per the AISC 341-22 protocol, expressed in terms of story drift.

The equivalent story drift was determined as the tip displacement of the beam divided by the length of the beam as measured from the beam tip to the centerline of the column. This is consistent with AISC 341-22, as well as how the drift was determined in the UCSD test program (Ozkula et al. 2019). The beam and column were modeled with the properties of A992 Grade 50 (345 MPa) steel, whereas the ESW weld bulb was modeled to occupy the entire region bounded by the continuity plate, containment plates, and the column wall. The model included large strains and geometric nonlinearity, along with appropriately scaled imperfections to induce local buckling. A procedure outlined by Elkady and Lignos (2018) was used to determine the imperfections. Within this procedure, the mode shapes were determined through eigenvalue analysis, whereas the amplitudes were d/250 for the web out-ofplane imperfection (for a beam depth) d and $b_f/250$ for the flange out-of-plane imperfection (for a flange width b_f).

The global model utilized 37,000 hexahedral (i.e., C3D8R, C3D20R, and C3D20) elements to simulate the beam, column as well as all attached plates, i.e., the continuity plates and containment plates. This results in element sizes ranging from ~1 mm (in the vicinity of the notch) to ~100 mm over the length of the beam or column. These considerations were based on previous studies, i.e., Myers et al. (2009) on welded column base connections and Stillmaker et al. (2015) on welded column splice connections,

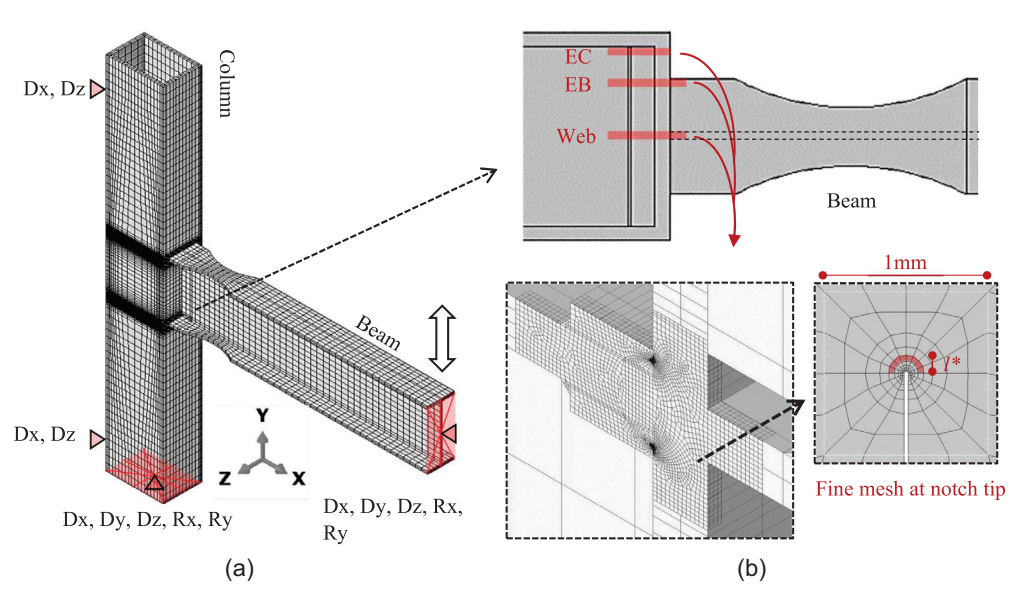


Fig. 6. Continuum finite-element models: (a) global model showing boundary conditions; and (b) local model.

which were highly successful in predicting fracture in welded connections that are in many aspects similar to the connections studied herein.

Figs. 7(a–d) compare results from tests with those from counterpart simulations. These comparisons provide validation of the modeling approach. Specifically, Figs. 7(a and b) compare the load-deformation curves [Fig. 7(a)] and the deformation patterns [Fig. 7(b)] between UCSD Specimen 3 and Simulation 6, which are complementary. Figs. 7(c and d) are similar, except they show data from UCSD Specimens 1 and 2, which are nominally identical in terms of global parameters, compared with Simulation 5, which is complementary.

Referring to Figs. 7(a and c), the overall match between the experimental and simulated load-deformation curves is reasonably good, and Figs. 7(b and d) indicate that the simulations are also able to capture the modes of local buckling. A closer inspection indicates that the simulated curves show slightly higher loads

compared with the experimental ones; this may be attributed to the fact that the experimental specimens undergo significant crack propagation during cyclic loading, which was not modeled in the simulations. Nonetheless, from the standpoint of providing a sense of the fracture demands at the unfractured ESW joint (which is the intent of this study), the simulations may be considered conservative because they overestimate the stresses in this region.

Fig. 6(b) illustrates the detail of a local model, shown for Simulation 6. The local features in ESW joint were modeled with significantly greater detail compared with the global model; this includes the containment plates bevels, as well as the gaps within them. The notch tip was simulated with a diameter of 0.025 mm which also reflects the width of the gap between the containment plate and the column wall (Fig. 6). This value is roughly 10% of the estimated critical crack-tip opening displacement (CTOD) for the material. McMeeking and Parks (1979) suggested that simulating the notch with this degree of acuity produces results comparable to

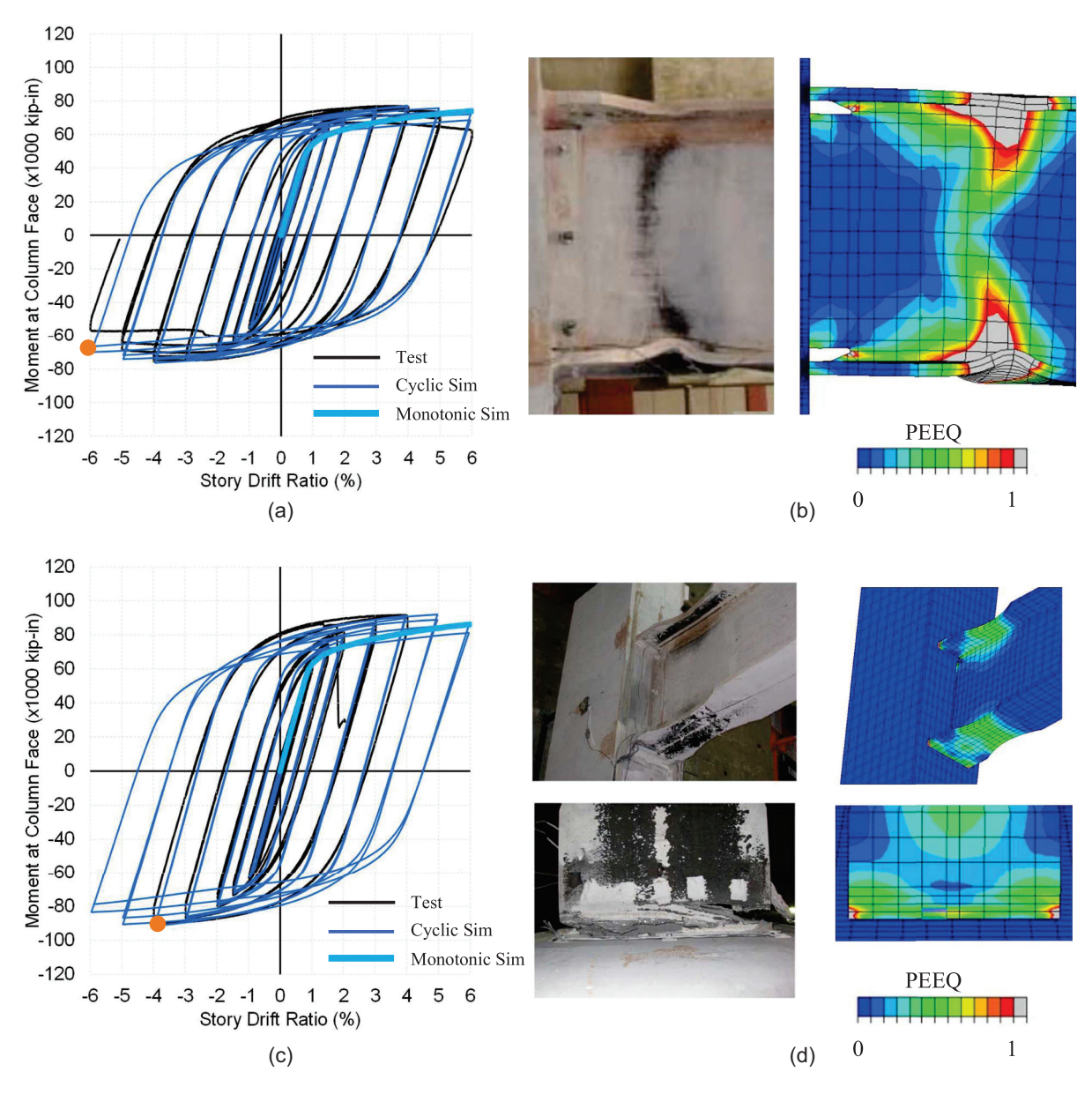


Fig. 7. Comparison between simulation and experimental data: (a) load-deformation response of UCSD Test 3; (b) deformations and plastic strains at instant shown by circle marker; (c) load-deformation response of UCSD Specimen 1; and (d) deformations and plastic strains at instant shown by circle marker.

those with perfectly sharp cracks. Previous studies (Stillmaker et al. 2015; Kanvinde et al. 2008) suggested that modeling weld root flaws as perfectly sharp cracks is appropriate. Referring to Fig. 6, the representation of the notch in this manner necessitates the use of a fine mesh, in which elements are on the order of 0.005 mm in size.

As discussed previously, the local model may be inserted at any location within the width of the connection (e.g., at the centerline of the beam, in line with the web) or toward the tips of the beam flanges to interrogate the fracture demands at those locations. This insertion implies that the deformation field (obtained from the global model at the location of interest) is used to drive the simulation of the local model. In this study, the local models were inserted at three locations within the global model (i.e., at the centerline, denoted Web, at a location in line with the edge of the beam flange, denoted EB, and at the edge of the column face plate, denoted EC) to interrogate the fracture demands at these locations (Fig. 6). The fracture indices used to quantify demands are summarized in a subsequent section.

Simulations to Examine Fracture Demands in Beam-Flange Groove Weld

Fig. 8 shows a CFE model corresponding to simulations in Table 2, which examine the necessity of specifying the continuity plate. The purpose of the continuity plate is to transfer the forces from the beam flange into the column without excessive out-of-plane bending or stress concentration in the column face plate, which may lead to fracture in the beam-flange groove weld. Referring to Table 2, a total of three parameters were assessed for this situation, featuring combinations of the continuity plate thickness (including absence of the continuity plate) and the column-wall thickness; these variables were anticipated to most strongly influence the stress–strain field in the beam-flange groove weld. Consequently, the need for the continuity plate was assessed based on the fracture toughness demands in this groove weld.

These simulations are similar in terms of overall construction to the ones for the ESW joint discussed previously, with some differences. A range of column-wall plate thicknesses is chosen relative to the current limit t_{cf-WF}^{AISC} for wide-flanged columns [Eq. (1)]. Only some of these simulations contain the continuity plates.

Two continuity plate thicknesses are selected, where one represents the minimum required for a single-sided connection with a wide-flanged column as per AISC 341-2022, i.e., $0.5t_{bf}$, and another is t_{bf} to examine if the stress distribution in box-column connections imply different limits compared with a wide-flanged column. In these simulations, the purpose of the continuity plate is to generate a benchmark estimate of fracture demands in the beam-flange groove weld, relative to which the demands from the simulations without the plate may be evaluated.

In the simulations with the continuity plate, the internal joint between the continuity plate and the column-wall plate is modeled simply as a tie constraint, without the complexity of the ESW detail or the containment plates, because the detail in the ESW region does not influence the stress or strain state in the beam-flange groove weld. In all simulations (i.e., with and without the continuity plate), the beam-flange groove weld is modeled as shown in Fig. 8, based on typical dimensions used in similar CFE studies previously (e.g., Skiadopoulos and Lignos 2022). Second, the details reflect a post-Northridge detail such that there are no backing bars or other discontinuities in the flange groove weld area. Consequently, the fine meshes (and the associated transitions) are not needed for these models as they are for the ESW joints.

Fig. 8 shows the mesh in this region; the elements are all C3D8R and on the order of 0.5 mm. A mesh convergence study indicated that this degree of mesh refinement is sufficient to capture the strain and stress gradients in the region. Because the fine meshing around the notch tip is not needed, only global models were constructed for this set of simulations.

Simulation of Material Constitutive Response

For all materials (i.e., beam, column plate, and ESW bulb or beam-flange groove weld), a von Mises plasticity model with combined isotropic kinematic hardening (specifically, the Frederick and Armstrong 1966) model was used. Based on previous studies (e.g., Elkady and Lignos 2018; Skiadopoulos and Lignos 2022; Tsai et al. 2020), these models are able to represent the constitutive response of these materials with sufficient accuracy. Table 3 summarizes the parameters used for the model. The footnotes of Table 3 describe the role of each parameter; the full description of the

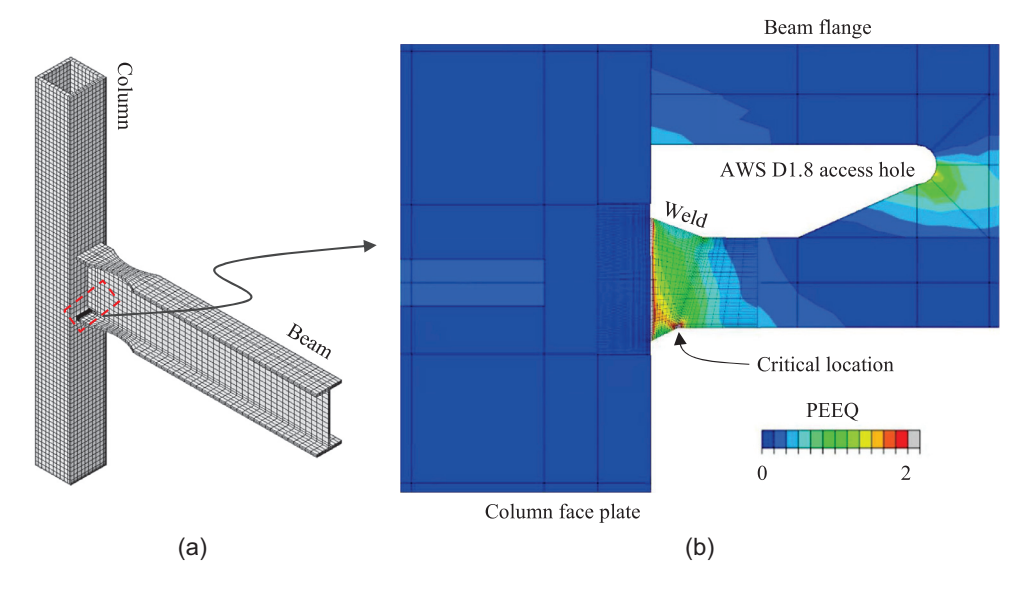


Fig. 8. Continuum finite-element model of simulations to examine fracture toughness demands in beam-flange to column groove weld outside the box column.

Table 3. Material constitutive parameters

Input material properties			Continuity		_
(ABAQUS)	Beam	Column	plates	ESW	HAZ
Yield stress, F_{y} (MPa)	410	412	427	464	489
Tensile strength, F_u (MPa)	521	564	575	563	586
Q_{∞} (MPa) ^a	89.6	130	130	103	103
B^{b}	12.0	7.69	7.69	5.00	5.00
C (MPa) ^c	3,376	3,318	3,318	1,450	2,140
γ^{d}	20.0	16.9	16.9	8.00	11.5

^aMaximum possible increase in yield surface size under isotropic hardening.

constitutive model has been given by Smith et al. (2017). The parameter selection for these was conducted based on the following:

- Column plate base material, beam base material, and containment plate material values were adopted directly from Ozkula et al. (2019).
- Electroslag weld and groove weld values were calibrated to the
 cyclic stress strain data obtained by Myers et al. (2009) for allweld E70 weld assemblies. These match results of microprobe
 testing by Ozkula et al. (2019), which reported discrete yield
 and ultimate values in a monotonic sense.

Anisotropy in material properties, which arises due to directionality of the welding, was not considered. Finally, the constitutive properties of the HAZs were not directly modeled as a separate zone. This appears to be an acceptable approach acknowledging the uncertainty in its spatial extent, and is based on previous simulation studies by Kanvinde et al. (2008), as well as Myers et al. (2009).

Fracture Indices Used to Interpret Results of the CFE Models

Fracture demands were monitored through two indices. One was the contour J-integral, which provides a measure of the crack driving force or fracture toughness demand under monotonic loading, whereas the other was a continuum damage mechanics—based model, specifically, the stress-weighted damage fracture model (SWDFM) (Smith et al. 2021), which is able to characterize the damage under cyclic loading and ultralow-cycle fatigue (ULCF) (Kanvinde and Deierlein 2007), which occurs during earthquake-type loading. Both these measures were used for the details with the ESW, which has a relatively sharp notch as shown previously. Only the SWDFM was used for the simulation models without the ESW (i.e., those summarized in Table 2) because these do not contain a sharp notch and are subject to large-scale yielding over the beamflange groove weld region. The calibration and implementation of these fracture measures is now described.

Contour J-Integral

The contour J-integral (Rice 1968) was determined for each of the notch tips produced by the containment plates. The J-integral (denoted J_I where the subscript denotes Mode I crack opening) is an indicator of the crack driving force or fracture toughness demands produced by the notch under monotonic loading. Consequently, these calculations are performed only for the monotonic cases. Specifically, the J-integral contours are determined along multiple locations along the front of the notch, which extends along the length of the ESW joint. At each of these locations, standard procedures (implemented within ABAQUS) were used to determine J_I ; a total

of seven contours were used to achieve a stable value of J_I following best practices outlined by Jhunjhunwala and Kanvinde (2023). The J-integral determined in this manner may be converted to an equivalent stress-intensity factor K_I as per the following relationship:

$$K_I = \sqrt{\frac{EJ_I}{(1 - \nu^2)}} \tag{2}$$

where ν = Poisson's ratio (taken as 0.3 for steel); and E = elastic modulus. For the simulations conducted in this study (i.e., considering all the parameter sets), the value of K_I at any location along the crack front was in the range of 15–120 MPa \sqrt{m} at an applied equivalent interstory drift of 4%. This is significantly lower than typical K_{IC} values for steel base as well as weld materials (including ESW welds) that are in the range of 206–486 MPa \sqrt{m} . These, in turn are based on Charpy V-notch (CVN) material testing from the Ozkula et al. (2019) study, converted to equivalent K_{IC} values using the Barsom and Rolfe (1999) correlation as per a process outlined by Jhunjhunwala and Kanvinde (2023).

This preliminary comparison suggested that from a pure fracture mechanics standpoint, the toughness demands produced by the notch are somewhat unlikely to directly produce fracture under monotonic loading. This was examined more rigorously using a weakest-link approach that determines the probability of failure of the weld considering that properties may vary along the length of the weld, with the weakest link controlling. The approach is based on work by Beremin et al. (1983), synthesized by Jhunjhunwala and Kanvinde (2023). As per this approach, the probability of fracture at any location along the crack front may be expressed

$$P_f = 1 - \exp\left\{-\int_0^{L_{\rm ESW}} \left(\frac{K_I(x) - K_{\rm min}}{K_0 - K_{\rm min}}\right)^4 dx\right\}$$
 (3)

where $K_I(x)$ = toughness demand at any location x along the length of the ESW, which is denoted $L_{\rm ESW}$; K_0 = parameter in the Weibull distribution and connotes fracture toughness with 63.2% fracture probability of exceedance; and $K_{\rm min}$ = lower threshold for fracture toughness. The values for these parameters were taken as $K_{\rm min}$ = 20 MPa $\sqrt{\rm m}$ and K_0 = 224 MPa $\sqrt{\rm m}$. These are representative values based on work by Jhunjhunwala and Kanvinde (2023).

When estimated in this manner, the probabilities of failure P_f (considered across all the simulations) at an interstory drift of 4% are in the range of 0% to ~7%, except for one situation (Simulation 2 with the large eccentricity) for which the probability is 84% (Table 1). The only other cases where there is a nonnegligible probability of failure correspond to Simulations 1 and 9, both of which have the Standard bevel. This further suggests that fracture

^bParameter controlling the rate of increase of the yield surface under isotropic hardening with respect to equivalent plastic strain.

^cParameter controlling linear kinematic hardening.

^dRecall term controlling the saturation value of kinematic hardening.

of the detail under monotonic loading without preaccumulated damage is generally unlikely except when the unintended eccentricity is large or if an improved bevel is used. In fact, experimental data from both the US (Ozkula et al. 2019) and Taiwan (Tsai et al. 2020) appear to corroborate this, wherein fracture was observed only after significant cyclic loading, even if the net stress (or load) demands did not increase from cycle to cycle.

Stress Weighted Damage Fracture Model

Whereas the J-integral is an indicator of the crack driving force (or energy release rate) ahead of sharp crack under monotonic loads, it is not a valid index to assess ULCF (Kanvinde and Deierlein 2007), which occurs under seismic loading, as wells as the cyclic loading histories applied to the models. Continuum damage mechanics models have been shown to predict ULCF fracture (Kanvinde and Deierlein 2007; Berdin and Besson 2004) with good accuracy. In this study, one such model, i.e., SWDFM (Smith et al. 2021), is used to assess fracture. The SWDFM is based on the micromechanics of ULCF and has been extensively validated against both coupon (Smith et al. 2021) and full-scale (Zhu et al. 2021) test data. Unlike the J-integral, SWDFM is determined at each continuum location in the vicinity of the notch tip, as well as over the entire joint, and is able to track the progression of damage during cyclic loading. The SWDFM predicts ULCF fracture to initiate if

$$D = C_{\text{SWDFM}} \int_0^{\varepsilon_p} (2 \exp(1.3T) - \exp(-1.3T))$$

$$\times \exp[k_{\text{SWDFM}}(|X| - 1)] d\varepsilon_p \ge 1 \tag{4}$$

where D= damage, which must exceed unity over a material length scale defined by the parameter l^* , usually taken as 0.1 mm, based on numerous studies (Kanvinde and Deierlein 2007; Ziccarelli et al. 2023). The damage is determined by numerically integrating the function on the right-hand side of Eq. (4) that weighs two stress invariants, namely stress triaxiality $T=\sigma_m/\sigma_{\rm eff}$ (the ratio of the mean stress σ_m to the von Mises stress $\sigma_{\rm eff}$), and the Lode parameter X over the entire loading history. The Lode parameter is related to J_3 , i.e., the third invariant of the stress tensor, and J_2 (the second invariant), such that $X=3\sqrt{3}\cdot J_3/(2\cdot J_2^{3/2})$, distinguishing stress states from axisymmetric $(X=\pm 1)$ to plane strain (X=0).

The terms $C_{\rm SWDFM}$ and $k_{\rm SWDFM}$ are material parameters that must be calibrated to test data using coupon tests. Because such coupon data were not available for this study, best estimates of the $C_{\rm SWDFM}$ and $k_{\rm SWDFM}$ parameters were developed based on previous studies. For ESW welds, Tsai et al. (2020) reported parameter calibration for a continuum damage mechanics model [the cyclic void growth model (CVGM)] developed previously by Kanvinde and Deierlein (2007).

SWDFM is a major improvement over CVGM in capturing the effect of the Lode parameter, which the CVGM does not see a comparative analysis between the two models by Smith et al. (2021). However, an equivalence between parameters may be established by equating the damage functions for both models over the stress histories used in the calibration tests. Specifically, in the CVGM [which is used by Tsai et al. (2020)] the damage is defined

$$D_{\text{CVGM}} = \int_{0}^{\varepsilon_{p}^{\text{critical}}} \frac{\exp(1.5T)}{\eta_{\text{mono}}^{\text{critical}}} d\varepsilon_{p}$$

and does not contain the dependence on the Lode parameter X. On the other hand, damage as interpreted by the SWDFM (used in this study) is defined as D shown in Eq. (4), and contains the Lode parameter.

The process used to estimate the SWDFM parameter C_{SWDFM} based on the Tsai et al. (2020) work was as follows. First, finiteelement simulations were conducted complementary to the circumferentially notched tensile coupon tests of Tsai et al. (2020), based on material data and geometries reported by them. These finiteelement simulations followed best practices outlined previously (Myers et al. 2010). The stress and strain histories arising from these simulations were used to compute the damage functions of both the SWDFM [Eq. (4)], and the CVGM. Then, the instant of fracture in the tests was determined by using the value of $\eta_{\text{mono}}^{\text{critical}}$ and setting the CVGM damage function equal to unity. Finally, the SWDFM damage function was integrated up to this instant and also set equal to unity to determine C_{SWDFM} . For the SWDFM, the term corresponding to the Lode parameter $\exp[k_{SWDFM}(|X|-1)]$ becomes unity because the Lode parameter X = 1 due to the axisymmetric stress state present in the circumferentially notched tensile coupons.

This exercise was conducted for the HAZ, which is determined to be the least tough material as per testing by Tsai et al. (2020). For this material, a value $\eta_{\rm mono}^{\rm critical}=0.704$ [as reported by Tsai et al. (2020)] resulted in a $C_{\rm SWDFM}$ value of 0.907. This is also the region where ULCF fracture initiates and propagates in the tests considered in this study, e.g., Fig. 3. Similar calibration studies were conducted by Myers et al. (2009) for the HAZ in toughness-rated FCAW groove welds that reflect post-Northridge construction (e.g., AISC 341-22). Based on these calibration studies, the $C_{\rm SWDFM}$ value is estimated as 0.399.

The parameter k_{SWDFM} , which controls the Lode dependence, cannot be independently calibrated from these studies because they all feature axisymmetric specimens for which X = 1 (i.e., there is only one value of X). Consequently, a characteristic value of $k_{\text{SWDFM}} = 0.5$ (Smith et al. 2021) was used in this study for both the FCAW and ESW materials. The subjectivity in estimating these parameters is acknowledged; as a result, it is somewhat challenging to extrapolate results to significantly different materials or geometries. Nonetheless, this is deemed acceptable in the context of this study because (1) the overarching aim of the study is to examine the fracture susceptibility of different details in relative, rather than an absolute sense, and (2) a range of fracture parameters (in the vicinity of the best estimates) is used to conduct a sensitivity study, which is used to support the interpretation of results. The SWDFM was monitored only for the cyclic simulation runs because the damage from SWDFM is extremely low if the connection is loaded monotonically.

Results and Discussion

The conventional fracture mechanics index (i.e., J-integral) indicated that the likelihood of fracture of the ESW joint under monotonic loading was exceedingly low (P_f values tabulated in Table 1). As a result, the results and discussion focus on the continuum damage mechanics based damage (as obtained from the SWDFM). Fig. 9 plots the evolution of damage in the simulations (from Table 1), using the parameters $C_{\rm SWDFM} = 0.907$ and $k_{\rm SWDFM} = 0.5$. Each curve represents a location through the width of the ESW weld. Within each curve, the plotted damage represents the damage D as determined from Eq. (4) at distance of I^* from the notch tip in the angular direction where it is the maximum. This respects the SWDFM criterion including the characteristic length.

Although shown in Fig. 9 for the details with the ESW joint (i.e., from Table 1), similar damage evolution plots were also generated for the simulations where the beam-flange groove weld was investigated (i.e., from Table 2). For the ESW simulations, the

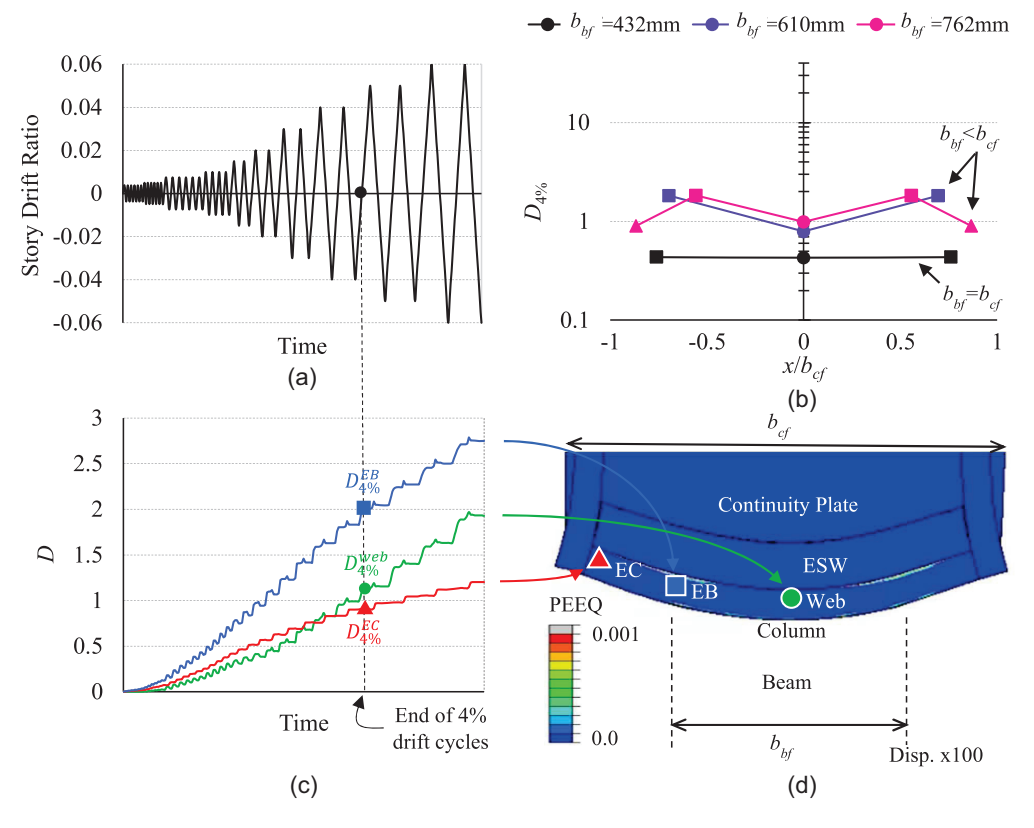


Fig. 9. Damage evolution in ESW weld: (a) loading protocol; (b) damage profile along the weld length at 4% drift; (c) temporal evolution of damage; and (d) locations at which damage is recorded.

damage was monitored at three locations along the ESW joint (Web, EB, and EC as shown in Fig. 6) for the cases where the beam flange is less wide compared with the column flange; these are distinguished by the square, triangle, and circle markers, respectively, in Fig. 9(d). When the beam flange was as wide as the column flange, damage at only two locations (i.e., Web and EB) were monitored.

Referring to Figs. 9(c and d), the damage at EB locations tended to be higher than that at Web and EC. This is due to a stress concentration that occurs due to the out-of-plane bending of the column wall and the discontinuity introduced by the edge of the beam flange. Fig. 9(c) also indicates the damage corresponding to the end of the 4% drift loading cycles in the loading protocol. This instant in the loading history is particularly relevant because the 4% drift is associated with acceptance criteria for moment connections as per AISC 341-22 (80% of the beam nominal moment strength must be maintained at this value). The damage values at this instant were retained and denoted $D_{4\%}^{\rm web}$ for the damage at the center (i.e., in line with the web), $D_{4\%}^{\rm EB}$ for damage at edge of the beam, and $D_{4\%}^{\rm EC}$ for damage at edge of the column.

Similar damage evolution curves were generated for the simulations in Table 2 as well. In these, the damage was monitored at every location along the groove weld, and the highest value at any instant was recorded. Similar to the ESW simulations, damage values $D_{4\%}$ were recorded for these simulations as well. For these simulations, the damage tended to be higher at edge of the groove weld near the tips of the flange.

A comparison of the $D_{4\%}$ values across the various configurations provides a direct way to assess the fracture performance of various details both in an absolute sense, and also relative to each other in the context of acceptance criteria for such connections.

To this end, Figs. 10(a-g) plot the damage terms $D_{4\%}^{\text{Web}}$, $D_{4\%}^{\text{EB}}$, and $D_{4\%}^{\text{EC}}$ (where applicable) against each parameter of interest from in Table 1 (i.e., for the ESW welds). A similar figure was plotted, as detailed subsequently, for the simulations in Table 2.

Each subfigure evaluates the effect of a single parameter. For example, Fig. 10(a) plots the damage values $D_{4\%}$ against the different types of bevel detail. The bars of similar shading indicate configurations that are otherwise identical, except for the primary variable plotted on the horizontal axis; consequently, a comparison between bars of the same shading isolates the effect of the primary variable. The points on each bar represent the damage at different locations (Web, EB, and EC) for each of the simulations. Referring to Figs. 10(a-g), some parameters clearly have a much larger effect on the fracture demands. Table 1 also includes information regarding the drift at which the damage first exceeds 1.0 at each location, indicating the drift at which fracture would initiate.

Based on Table 1 and Figs. 10(a–g), the following observations may be made:

• Referring to Fig. 10(a), the type of containment plate bevel detail has a major effect on the fracture demands. Specifically, the conventional containment plate without the bevels results in damage at all locations along the flange that is two to five times larger than both B1 and B2 (i.e., the US and Taiwan bevels). However, the simulations only captured the geometric differences between the bevels, and not material effects that may be generated due to different cooling rates (e.g., between Bevel B1 with the shims, and B2 without). Further, the absolute values of the damage indicate that only the B1 and B2 conditions are even viable, i.e., the damage is in the neighborhood of 1; the damage with the S-type bevel is roughly an order of magnitude higher. This is consistent with experimental data in the US (Fig. 3),

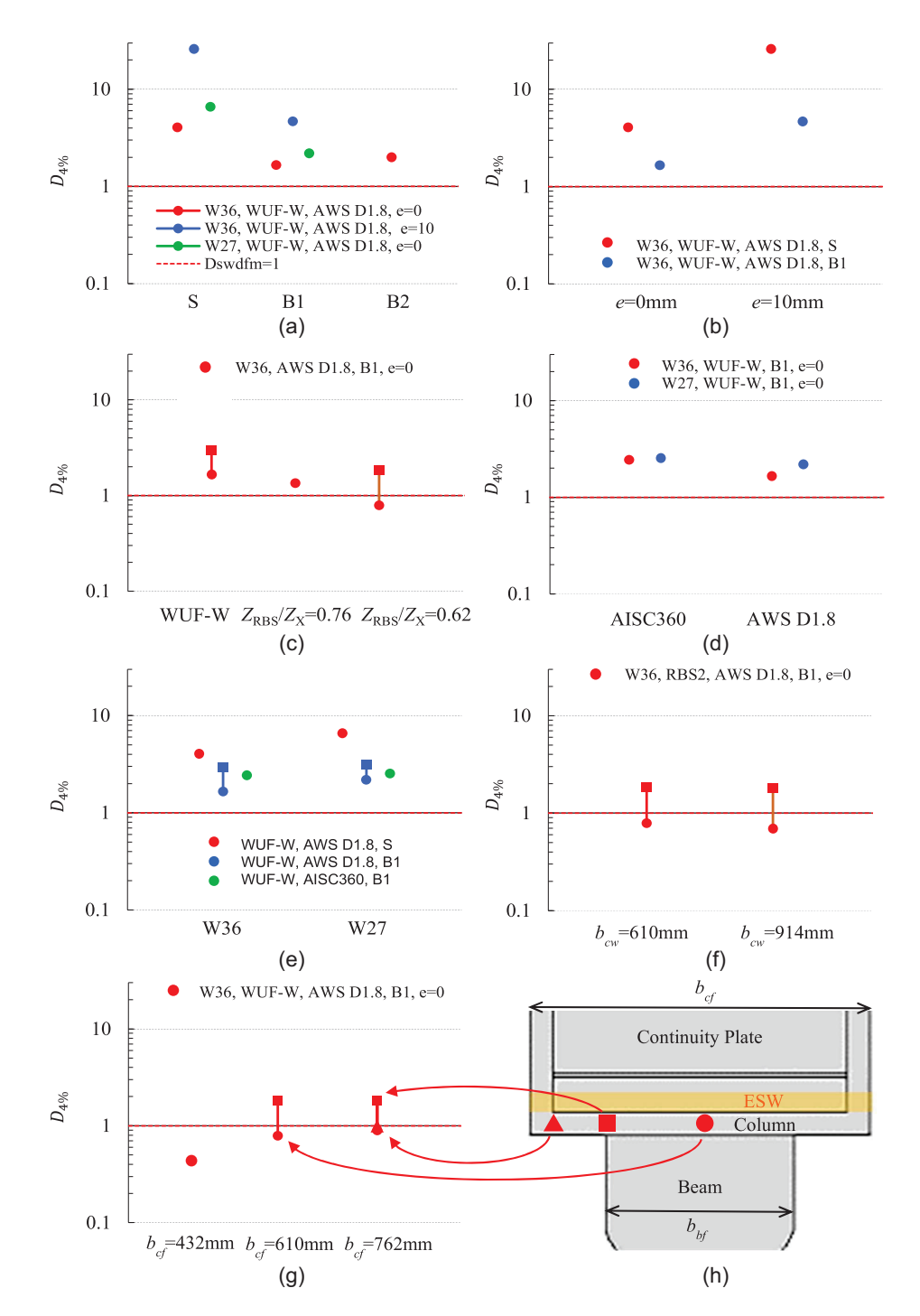


Fig. 10. Damage at 4% drift plotted against parameters of interest: (a) bevel detail; (b) weld bulb eccentricity; (c) section reduction; (d) WAH detail; (e) beam size; (f) column depth; (g) column width; and (h) illustration showing where each marker was obtained.

which indicates the initiation of fracture in every specimen that has been tested in the US, with these details.

• An examination of Table 1 (columns titled Drift when D = 1) indicates that in most specimens, fracture initiates (i.e., the damage exceeds 1.0) for drifts in the range of 0.5% to 6% (with a median value of 2%). This suggests early initiation of fracture in most of the simulations. In fact, the only simulation where the fracture initiation drift was greater than 4.0% (considering damage at all locations) is Simulation 13 (in which the damage remained below 1.0 for the entirety of loading). In this simulation, the beam-flange width and the column width are exactly the same. In general, this is difficult to achieve in practice. However,

from a behavioral standpoint, this appears to be extremely beneficial because it prevents the out-of-plane bending of the column wall and greatly mitigates the stress concentration shown previously in Fig. 9(d). In fact, as noted in Fig. 9(b), this results in uniform damage through the length of the ESW, which is by far the lowest among all the simulations. This suggests that stiffening the column flange from the outside, by either having a wide beam flange or other details should be explored as a means to improve connection performance.

• Referring to Fig. 10(b), the eccentricity of the weld bulb has a major effect on the fracture demands as well, i.e., an eccentric bulb (with e = 10 mm) produces demand nearly three to six

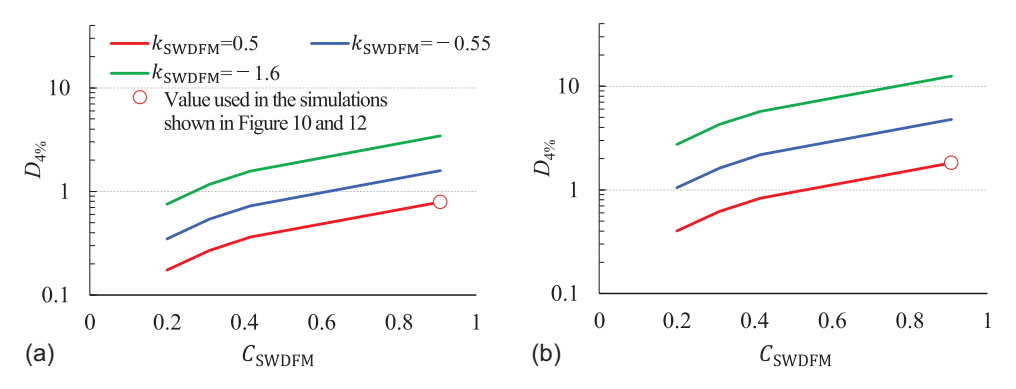


Fig. 11. Sensitivity of estimated damage to material parameters of the SWDFM at two locations: (a) location web; and (b) location EB.

times the centered bulb. This does not consider the eccentricity of the continuity plate with respect to the beam flange, which [as shown by Tsai et al. (2020)] has an even larger influence on toughness demands, indicating that alignment tolerances for both the continuity plate and the weld itself are critical for a successful connection detail.

- The use of the RBS detail to reduce stress demands at the ESW also appears to be a highly effective strategy, such that the reduction in the Z_{RBS}/Z from a value of 1.0 (i.e., a WUF-W connection) to 0.62 resulted in a decrease of damage values by 40%-50%.
- Three parameters have only a modest influence on fracture demands. These include (1) the weld access hole detail with the AWS D1.8 detail resulting in slightly lower fracture demands (~10%-15% lower) compared with the AISC 360 detail [Fig. 10(d)], (2) the beam depth [Fig. 10(e)], and (3) the column size [Figs. 10(f and g)]. Of these, the insensitivity to column size is particularly important because, as per AISC 358 (AISC 2022a), column depths in box-column connections are limited to 24 in. (610 mm). The simulations indicate that increasing the column size does not result in a significant change in fracture demands. This provides support for larger column sizes that may reduce material costs by reducing plate thickness.

In summary, the simulation results suggest that the most favorable conditions to minimize the potential of fracture may be achieved through a combination of (1) using improved bevel details, i.e., either the B1 or B2 type, (2) reduction of demands using RBS details, (3) enforcing strict tolerances for alignment between the plates and weld bulb eccentricity with respect to the plates, and (4) using beams with flanges that are as wide as the columns. Additionally, the use of improved weld access hole details is somewhat useful. It is useful to study the most favorable combination of parameters for which test data exist. This combination corresponds to Simulation 6 from Table 1, which corresponds to UCSD Specimen 3). For this condition, $D_{4\%}^{\text{web}}$ is 0.79 and $D_{4\%}^{\text{EB}}$ is 1.8. In the context of these observations, the following points were noted.

First, despite favorable parameters from a geometric standpoint, the presence of the notch effect (in combination with the local material toughness properties) is likely to initiate ductile (or ULCF) type fracture at some point in the ESW, even if it does not propagate. This is consistent with experimental response in which all UCSD tests showed some extent of ductile initiation and propagation. The transition of these ductile cracks to brittle cleavage is a random process (Beremin et al. 1983), whose probability grows as the ductile crack propagates. In two out of the three UCSD specimens, such propagation occurred.

Second, it is important to note that the values of damage listed in Table 1 and shown in Figs. 10(a–g) use a single set of values for

the SWDFM material parameters (i.e., $C_{\rm SWDFM}=0.907$ and $k_{\rm SWDFM}=0.5$) based on the estimates outlined previously. To assess the sensitivity of damage to these, Figs. 11(a and b) plot the value of damage at 4% (for Simulation 6; the trends for other simulations are similar), i.e., $D_{4\%}$ against the $C_{\rm SWDFM}$ for three different values of $k_{\rm SWDFM}$. Fig. 11(a) plots the damage at the centerline location, whereas Fig. 11(b) plots the damage at EB location. The range of $C_{\rm SWDFM}$ shown in these figures, as well as the values of $k_{\rm SWDFM}$, represent the typical values noted in the literature for similar steel materials (Zhu et al. 2021). Also indicated in these figures are the values used to determine the damage values shown in Figs. 9, 10, and 12.

Referring to these figures, it is evident that the damage is fairly sensitive to the selection of material parameters. This has two implications. First, is it important to characterize local material properties with accuracy for effective simulation and prediction of fracture performance. Second, and perhaps more important, is that in addition to improvement of geometric parameters, the enhancement of local material toughness (e.g., through filler metal selection) or weld-process modification has the potential to significantly prevent fracture.

The results of the simulations to examine the necessity of the continuity plate are presented in Table 2 (last column) and Fig. 12. Table 2 indicates the value of the damage $D_{4\%}$ determined for each of the simulations; this is the maximum value at any location along the length of the groove weld, i.e., the width of the beam flange. In general, the maximum damage for both the simulations with and without the continuity plate occurred at the edge of the beam flange. From the last column of Table 2, it is immediately apparent

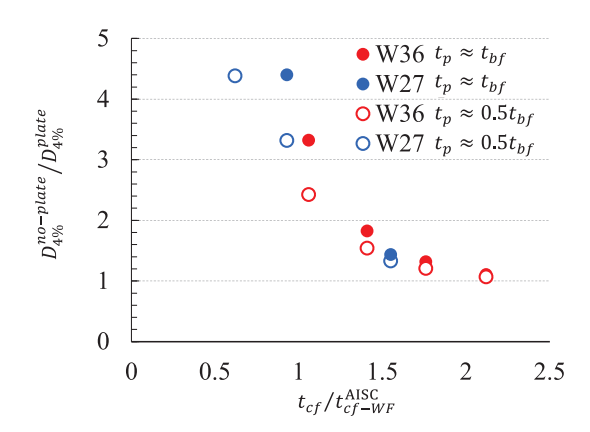


Fig. 12. Effect of column flange (wall) thickness on fracture toughness demand relative to the condition with the continuity plate.

that the damage in configurations with the continuity plate is generally lower than the damage without the continuity plate. Further, it is apparent that the damage values for the configurations with continuity plate are lower than 1.0 (i.e., the groove weld is generally not susceptible to fracture) except for Simulation 17.

Fig. 12 plots the ratio of these two damage values (i.e., without and with continuity plate) for each of the configurations that are otherwise identical. These ratios are plotted against the ratio $t_{cf}/t_{cf-WF}^{\rm AISC}$, which indicates how thick the column flange is relative to the AISC limit (AISC 341-22 for wide-flanged columns) at which the continuity plate is not required. These data are plotted for the two values of the continuity plate thickness (i.e., $t_{bf}/2$ and t_{bf}). The former is the requirement for single-sided connections as per AISC 341-22, but the latter (i.e., thicker continuity plate) is provided as an additional parametric variable, recognizing that the stress flow in box columns may be more adverse because the column web is not present behind the beam web.

Referring to Fig. 12, a clear trend is noted between the ratio $D_{4\%}^{\text{no-plate}}$ and $D_{4\%}^{\text{plate}}$ for all the configurations, i.e., combinations of beam size and continuity plate thickness (suggesting that the trend itself is independent of the configuration). Specifically, as the t_{cf} increases, the ratio $D_{4\%}^{\text{no-plate}}/D_{4\%}^{\text{plate}}$ approaches 1.0, indicating that the continuity plate has a decreased effect on lowering the strains (a value close to 1.0 indicates that the continuity plate is not needed). Interestingly, at the $t_{cf}/t_{cf-WF}^{\text{AISC}}$ value of 1.0, $D_{4\%}^{\text{no-plate}}/D_{4\%}^{\text{plate}}$ is in the range of 2.4 to 4.4. This suggests that criteria for the use of continuity plates in wide-flanged sections is not applicable to box-column connections. This is not unexpected, because unlike beam-column connections with wide-flanged columns, the box columns do not include a web directly in line with the beam web, resulting in a more adverse stress flow from the beam to the column flange.

Further examination of Fig. 12 indicates that for both continuity plates with thickness $t_{bf}/2$ (the minimum required for wideflanged column connections) as well as t_{bf} , the ratio $D_{4\%}^{\text{no-plate}}/D_{4\%}^{\text{plate}}$ approaches 1.0 only as $t_{cf}/t_{cf-WF}^{\text{AISC}}$ approaches 2.0. For all of these, the ratio $b_{fb}/b_{fc}=0.7$. This suggests that for box-column connections, the continuity plate requirement may need to be significantly more stringent compared with wide-flanged column connections.

Summary, Conclusions, and Limitations

Beam-to-box-column connections in seismically designed SMF buildings present special challenges that are not encountered in wide-flanged column connections. This study presented results of parametric finite-element simulations to examine relationships between configuration or geometric parameters that can be controlled in design and fabrication, and fracture demands. Two sets of simulations were conducted: one investigated the effect of various parameters on toughness demands in the ESW detail, whereas the second examined under what conditions it may be feasible to avoid the continuity plate altogether. The main insights from the simulations with the ESW welds include the following:

- Purely monotonic loading (without damage accumulated due to cyclic loading) appears unlikely to produce fracture in most of the details, except when the eccentricity of the weld bulb is large.
- In terms of design and fabrication variables, using an improved bevel detail and utilizing RBS significantly reduced the fracture demands. If ever possible in practical design, specifying a

- column width equal to the beam-flange width has the greatest potential for reducing demands because this minimizes out-ofplane bending of the column-wall plate.
- The eccentricity of the weld bulb has a major adverse effect on the fracture demands (three to six times larger damage); this is because the notch size increases as the weld bulb unintentionally moves to one side during welding. The implication is that weld fabrication tolerances are especially important in ESW welds in seismic box-column connections.
- Some variables (the weld access hole configuration, as well as beam depth and column size) were found to have only a minimal effect on fracture demands. Of these, the insensitivity to column size has important design implications because current guidelines [AISC 358 (AISC 2022a)] limit the column depth to 610 mm (24 in.).
- The damage is also highly sensitive to the assumed fracture toughness capacity, indicating that improvement of welding processes and materials will have a significant impact on connection performance.

The key finding from the simulations without the continuity plate is that current guidelines for the use of continuity plates (based on the flange thickness of wide-flanged columns) may be inapplicable to box columns. This is attributed to the absence of the column web in line with the beam web which results in an adverse stress flow from beam to column. The simulations suggest that using a column thickness limit two times as large as the current limit for wide-flanged sections may result in acceptable performance comparable to connections with a continuity plate.

It is important to interpret the results of this study in the context of its limitations, which are numerous. First, this is a finite-elementbased parametric study, and this results in significant idealizations about geometric tolerances and imperfections, for example, the representation of the containment plate notch as a sharp crack. The material properties (particularly the fracture toughness properties) were estimates based on correlations to CVN tests taken from specific locations, rather than direct measurements of these properties over the entire weldment, although this is addressed to an extent through a sensitivity study. In this regard, some effects were not modeled, e.g., the effect of shim plates (as in Bevel B2) was modeled only in terms of geometry, but not in terms of its effect on material properties. However, variations in material microstructure over small scales, even slight variation in the locations of these microstructures with respect to local stress concentrators such as the notches, and the effect of residual stresses may result influence the results. Residual stresses were not explicitly modeled in this study, based on observations in previous studies (e.g., Chi et al. 2000; Myers et al. 2009) that these may not influence fracture, especially when large cyclic inelastic deformations are present.

Additionally, the continuum damage mechanics—based model to represent ULCF itself is prone to a degree of error in calibration as well as in application, owing to effects such as mesh sensitivity of near-tip crack fields. Finally, although the simulation approach is well-validated against other connection types, only two experiments are available for the ESW connection. In light of these limitations, the most useful interpretation of the results is in a relative sense, wherein the fracture susceptibility of different configurations may be assessed relative to one another, rather than in an absolute sense (e.g., the estimated drift or deformation at fracture). The expectation is that such relative assessments, and the qualitative insights provided by this study will support further experimental verification, as well as weld processes and materials that ultimately result in greater confidence in these connections.

Data Availability Statement

Some or all data, models, or code that support the findings of this study are available from the corresponding author upon reasonable request.

Acknowledgments

The authors acknowledge support from the National Science Foundation (Grant No. CMMI 2129445). The authors are also thankful to Professor Michael Engelhardt of the University of Texas, Austin, for his constructive advice. The views and findings presented in this article are entirely of the authors.

References

- AISC. 2022a. Prequalified connections for special and intermediate steel moment frames for seismic applications. AISC 358-22. Chicago: AISC.
 AISC. 2022b. Seismic provisions for structural steel buildings. AISC 341-22. Chicago: AISC.
- AISC. 2022c. Specification for structural steel buildings. AISC 360-22. Chicago: AISC.
- AWS (American Welding Society). 2016. Structural welding code–seismic supplement. AWS D1.8/D1.8M. Doral, FL: AWS.
- Barsom, J. M., and S. T. Rolfe. 1999. Fracture and fatigue control in structures: Applications of fracture mechanics. West Conshohocken, PA: ASTM.
- Berdin, C., and J. Besson. 2004. *Local approach to fracture*. Paris: Les Presses de Ecole des Mines.
- Beremin, F., A. Pineau, F. Mudry, J. C. Devaux, Y. D'Escatha, and P. Ledermann. 1983. "A local criterion for cleavage fracture of a nuclear pressure vessel steel." *Metall. Trans. A* 14 (11): 2277–2287. https://doi.org/10.1007/BF02663302.
- Chen, C. C., C. L. Lai, and K. C. Lin. 2009. "Finite element analysis of electro-slag welding for diaphragms in steel box column." In Proc., 11th Taiwan-Korea-Japan Joint Seminar on Earthquake Engineering for Building Structures SEEBUS 2009, Kyoto, Japan: The Japan-Korea-Taiwan Joint Seminar on Earthquake Engineering for Building Structures.
- Chen, C. H., K. C. Lin, S. J. Jhuang, and H. Y. Chang. 2020. "Seismic performance evaluation of steel box-column connections with ESW stiffeners." *Int. J. Steel Struct.* 20 (Jun): 776. https://doi.org/10.1007/s13296-020-00321-9.
- Chi, W. M., G. G. Deierlein, and A. Ingraffea. 2000. "Fracture toughness demands in welded beam-column moment connections." *J. Struct. Eng.* 126 (1): 88–97. https://doi.org/10.1061/(ASCE)0733-9445(2000) 126:1(88).
- Elkady, A., and D. G. Lignos. 2018. "Improved seismic design and nonlinear modeling recommendations for wide-flange steel columns." *J. Struct. Eng.* 144 (9): 04018162. https://doi.org/10.1061/(ASCE)ST .1943-541X.0002166.
- Frederick, C. O., and P. J. Armstrong. 1966. *A mathematical representation of the multiaxial bauschinger effect*. Berkeley, UK: Berkeley Nuclear Laboratories.
- Gilmer, H. 2005. "Implementation of narrow-gap improved electroslag welding for bridge fabrication." In Proc., World Steel Bridge Symp. Conf. Proc., 2005. Chicago: American Institute of Steel Construction.
- Jhunjhunwala, A., and A. M. Kanvinde. 2023. "Fracture mechanics based fragility assessment of pre-Northridge welded column splices." J. Struct. Eng. 149 (6): 04023062. https://doi.org/10.1061/JSENDH .STENG-11749.
- JSSC (Japanese Society of Steel Construction). 2016. Guide book to prevent brittle fracture at an electroslag weld on the inner diaphragm. Tokyo: Japanese Society of Steel Construction.

- Kanvinde, A. M., and G. G. Deierlein. 2007. "A cyclic void growth model to assess ductile fracture in structural steels due to ultra low cycle fatigue." J. Eng. Mech. 133 (6): 701–712. https://doi.org/10.1061 /(ASCE)0733-9399(2007)133:6(701).
- Kanvinde, A. M., B. V. Fell, I. R. Gomez, and M. Roberts. 2008. "Predicting fracture in structural fillet welds using traditional and micromechanics-based models." *Eng. Struct.* 30 (11): 3325–3335. https://doi.org/10.1016/j.engstruct.2008.05.014.
- Lin, K. C., and S. J. Jhuang. 2010. "Seismic behaviors and design method on steel beam-to-box column connections with cover plate." [In Chinese.] Struct. Eng. 25 (2): 75–92.
- Lin, R. S., H. Y. Chung, and M. H. Lin. 2012. "Analysis and improvement for the inherent backing-bar crack problem of electrogas and electroslag welding in box-columns." [In Chinese.] J. Chin. Inst. Civ. Hydraul. Eng. 24 (2): 169–183.
- McMeeking, R. M., and D. M. Parks. 1979. On criteria for J-dominance of crack-tip fields in large scale yielding. ASTM STP 668. West Conshohocken, PA: ASTM.
- Myers, A. T., G. Deierlein, and A. M. Kanvinde. 2009. Testing and probabilistic simulation of ductile fracture initiation in structural steel components and weldments. Technical Rep. No. 170. Stanford, CA: Stanford Univ.
- Myers, A. T., A. M. Kanvinde, and G. Deierlein. 2010. "Calibration of the SMCS criterion for ductile fracture in steels: Specimen size dependence and parameter assessment." *J. Eng. Mech.* 136 (11): 1401–1410. https:// doi.org/10.1061/(ASCE)EM.1943-7889.0000178.
- Ozkula, G., R. Garai, P. Lee, and C. M. Uang. 2019. "Cyclic behavior of electroslag welded joints in beam-to-built-up box column steel moment connections." *J. Struct. Eng.* 145 (12): 04019146. https://doi.org/10.1061/(ASCE)ST.1943-541X.0002409.
- Padilla-Llano, D. A., and J. Ocel. 2021. "Qualification of electroslag welds made from HPS 485W (70W) and 345W (50W) steels." *J. Constr. Steel Res.* 183 (Aug): 106705. https://doi.org/10.1016/j.jcsr.2021.106705.
- Rice, J. R. 1968. "A path independent integral and the approximate analysis of strain concentration for notches and cracks." *J. Appl. Mech.* 35 (Mar): 379–386. https://doi.org/10.1115/1.3601206.
- Skiadopoulos, A., and D. Lignos. 2022. "Proposed backing bar detail in welded beam-to-column connections for seismic applications." *J. Struct. Eng.* 148 (8): 04022102. https://doi.org/10.1061/(ASCE)ST .1943-541X.0003374.
- Smith, C. M., A. M. Kanvinde, and G. G. Deierlein. 2017. "Calibration of continuum cyclic constitutive models for structural steel using particle swarm optimization." *J. Eng. Mech.* 143 (5): 04017012. https://doi.org /10.1061/(ASCE)EM.1943-7889.0001214.
- Smith, C. M., A. Ziccarelli, M. Terashima, A. M. Kanvinde, and G. Deierlein. 2021. "A stress-weighted ductile fracture model for steel subjected to ultra low cycle fatigue." *Eng. Struct.* 245 (Oct): 112964. https://doi.org/10.1016/j.engstruct.2021.112964.
- Stillmaker, K., A. M. Kanvinde, and C. Galasso. 2015. "Fracture mechanics-based design of column splices with partial joint penetration welds." *J. Struct. Eng.* 42 (2): 04015115. https://doi.org/10.1061/(ASCE)ST.1943-541X.0001380.
- Tsai, C. Y., K. C. Tsai, C. H. Li, C. C. Wu, K. C. Lin, and S. J. Jhuang. 2020. "Seismic fracture evaluation of diaphragm joints in welded beamto-box column moment connections." *Earthquake Eng. Struct. Dyn.* 49 (Jan): 1344–1362. https://doi.org/10.1002/eqe.3293.
- Yasumoto, H. 2023. "Fracture toughness demands in seismic moment frame connections of box columns." Master's thesis, Dept. of Civil and Environmental Engineering, Univ. of California.
- Zhu, Y., B. Fell, and A. M. Kanvinde. 2021. "Continuum damage mechanics based ductile fatigue-fracture prediction in buckling steel braces."
 J. Constr. Steel Res. 184 (Sep): 106812.https://doi.org/10.1016/j.jcsr.2021.106812.
- Ziccarelli, A., A. Kanvinde, and G. Deierlein. 2023. "Cyclic adaptive cohesive zone model to simulate ductile crack propagation in steel structures due to ultra-low cycle fatigue." Fatigue Fract. Eng. Mater. Struct. 46 (5): 1821–1836. https://doi.org/10.1111/ffe.13964.